IEEE Access
Multidisciplinary : Rapid Review : Open Access Journal

Received 23 February 2026, accepted 19 March 2026, date of publication 10 April 2026, date of current version 23 April 2026.

Digital Object Identifier 10.1109/ACCESS.2026.3682896

RESEARCH ARTICLE

EIRP-Based Ray Tracing Simulation and Experimental EMF Exposure Assessment of Operational 5G-NR MaMIMO Base Stations

JAVAD HEIDARI, (Graduate Student Member, IEEE),
WOUT JOSEPH, (Senior Member, IEEE), LUC MARTENS, (Member, IEEE),
AND GÜNTER VERMEEREN, (Member, IEEE)
Department of Information Technology, IMEC, Ghent University, 9052 Ghent, Belgium

Corresponding author: Javad Heidari (javad.heidari@ugent.be)

This work was supported by European Union's Horizon Europe Research and Innovation Program under Grant 101057622 (SEAWave).

ABSTRACT Accurate electromagnetic field (EMF) exposure assessment in operational fifth generation new radio (5G-NR) networks is challenging because most approaches rely on static or worst-case transmission assumptions, creating a gap between simulations and real-world measurements that this study bridges. We validate ray-tracing (RT) simulations for exposure estimation from 5G-NR massive multiple-input multiple output (MaMIMO) antennas operating in the 3.7–3.8 GHz frequency range 1 (FR1) band by integrating equivalent isotropically radiated power (EIRP) values recorded by base station antenna (BSA) counters. Using operational EIRP data enables realistic modelling of dynamic network behaviour and reduces uncertainty in line-of-sight (LOS) scenarios. In-situ EMF measurements performed according to IEC 62232 serve as a benchmark for evaluating simulation accuracy while considering the 4 dB target expanded uncertainty. Results show a median deviation of 1.6–3.8 dB between EIRP-based simulations and measurements, demonstrating good agreement, while the measured and estimated exposure levels remain well below International Commission on Non-Ionizing Radiation Protection (ICNIRP) limits, with a maximum of 0.6 %.

INDEX TERMS EMF exposure, ray tracing, 5G, MaMIMO, EIRP.

I. INTRODUCTION

The 5G networks represent a major advance in mobile communications, offering unprecedented data rates, ultra-low latency, and support for massive connectivity. These advancements are mainly driven by the application of millimeter wave (mmWave) frequencies and MaMIMO antennas, with beamforming techniques at its core [1], [2]. While the technical potential of 5G is transformative, it also introduces new challenges, particularly in understanding and assessing human exposure to EMFs.

The increasing deployment of 5G infrastructure necessitates rigorous evaluation of EMF exposure levels to ensure compliance with international safety guidelines and public health standards. This topic has become an essential field of study considering growing societal concerns regarding the potential health effects [3]. Organizations such as the ICNIRP [4] and the Institute of Electrical and Electronics Engineers (IEEE) [5] each provide their set of guidelines based on latest studies to mitigate health risks. The World Health Organization (WHO) [6], through its International EMF Project [7], assesses scientific evidence on the health effects of EMF exposure, identifies knowledge gaps, promotes research, develops exposure guidelines in collaboration with bodies like ICNIRP, and provides public guidance to ensure

The associate editor coordinating the review of this manuscript and approving it for publication was Su Yan.

global safety standards are met. However, the complexity of 5G networks introduces uncertainties in exposure estimation, driven by dynamic beamforming, diverse propagation environments, and user-specific factors such as mobility and user patterns [8]. Consequently, robust methodologies are required to accurately assess EMF exposure in real-world scenarios and validate predictive models with empirical measurements. Such efforts led to the development of the International Electrotechnical Commission (IEC) standards for evaluating human exposure [9] that are consistent and reproducible. In cases where time variations affects the selected metric, including fluctuations due to power control, beamforming (for MaMIMO), traffic load or duty cycle, the time-averaged metric is considered for comparison with the EMF exposure limits [9].

The literature, extensively covers exposure assessments for legacy wireless communication systems such as 2G, 3G, and 4G. In 5G, techniques ranging from empirical measurements [10], [11], and [12] to computational modelling [13], and machine learning [14] have been employed to characterize exposure levels in various environments. Previous studies have established baseline exposure metrics and demonstrated how network configuration, power-control strategies, and user density influence exposure levels [3], [8], [9], [10], [13]. However, the shift to 5G introduces new complexities that these approaches cannot fully capture. Advanced modelling is required, particularly because beamforming and MaMIMO produce highly directional, spatially non-uniform exposure patterns, and permanent beam steering in multiple directions. Traditional measurement campaigns and full-wave simulations, while accurate, are often impractical due to their significant time and computational demands. Deterministic approaches such as RT simulations offer an efficient alternative for modelling electromagnetic-wave propagation in complex urban environments. However, a key challenge in RT-based exposure assessment is the accurate representation of the transmitted power from BSAs, particularly for MaMIMO systems where the radiated power dynamically varies based on network load and beamforming patterns. Efforts to incorporate BSA counter data have shown that assuming a fixed beam and transmitted power led to an overestimation of exposure [15].

Numerous tools support RT for EMF simulations. Commercial platforms such as iBwave Design, MATLAB, Volcano, Wireless InSite, and WinProp provide comprehensive, high-accuracy propagation modelling. Open-source alternatives like Opal and Sionna offer accessible options, though typically with more limited functionality and accuracy [14]. The built-in ray tracing in MATLAB offers a key advantage by providing partial access to the underlying algorithms and individual rays, enabling power customization. This has been applied to city scale spatio-temporal simulations of 5G downlink (DL) exposure, using models capable of supporting large scale dynamic scenarios [13].

In this study, we propose a hybrid methodology that integrates the built-in RT in MATLAB and "Actual EIRP" data derived from BS counter measurements, henceforth referred to as EIRP data. The values extracted from EIRP data provide real-time information on the actual transmitted power and gain, which is used to assign the power and gain through EIRP values of all individual rays contributing to the total exposure at the evaluation point (EP). This approach enhances the exposure assessment by incorporating live network data rather than solely relying on generic transmission models or theoretical assumptions. This paper presents:

- **A hybrid methodology for 5G EMF exposure assessment** that integrates operational EIRP values, capturing transmitted power, antenna patterns, and traffic load—within ray-tracing simulations.
- **A parallel analysis of simulated and measured data** to validate the modelling approach and support the automation of exposure assessments.
- **A simulation-driven workflow** that provides a practical alternative to labour-intensive field measurement campaigns for regulators and operators.
- **An evaluation of typical uncertainty margins**, offering insights to guide future research and standardization efforts in EMF exposure evaluation.

These contributions provide a practical and scalable framework for assessing the exposure levels in operational 5G networks. The paper is structured as follows: Section II describes the methodology for 5G exposure assessment, with emphasis on RT and EIRP-based RT simulations, as well as the in-situ measurement setup and data collection criteria. Section III presents the simulation and measurement results along with a comparative analysis. Section IV concludes by summarizing the key findings.

II. METHODOLOGIES

In Belgium, information regarding base station (BS) deployments is publicly accessible through official databases, such as the one maintained by the Department of Environment [16]. The network analyzed in this study comprises sectorized, non-stand-alone 5G MaMIMO antennas operating in the n78 frequency band (3.7–3.8 GHz) [17], as detailed in Table 1.

For the purposes of this study, users are defined as user terminals (UTs) that maintain an active connection to the network and are engaged in data transmission or reception. In contrast, non-users refer to inactive UTs that are not currently involved in any data exchange.

The median GPS coordinate values were selected for each EP to ensure spatial consistency. Furthermore, all selected EPs are within region types classified as III-1,M, as defined in Annex A of [9].

A. RAY TRACING SIMULATIONS

Ray-tracing simulations are conducted in MATLAB R2024a using the Shooting and Bouncing Rays method [18]. The implementation leverages MATLAB's Antenna Toolbox [19] and Phased Array System Toolbox [20]. Throughout all

Table 1. Input parameters and configuration of raytracing simulation.

Symbol	Description	Value	Unit
Z_0	free-space impedance	377	Ω
f_c	carrier frequency	3.775	GHz
λ_c	carrier wavelength	7.93	cm
P_{TX}	conformity output power	42.8	dBm
$G_{TX}^{\max}$	conformity antenna gain	24.9	dBi
α	TX orientation in azimuth	150	°
h_{TX}	TX antenna height	32.75	m
$N_x \times N_z$	number of elements (×2)	12×8	—
$G_e^{\max}$	maximum element gain	8	dBi
HPBW_e	V/H-HPBW of element	65	°
d_e	interelement distance	$\lambda_c/2$	cm
$S_{\min}$	receiver sensitivity	−120	dBm
h_{RX}	receiver height	1.5	m
h_p	probe height	1.5	m
d_p	probe distance to UT	2	m
$N_R^{\max}$	Max number of reflections	5	—
$N_D^{\max}$	Max number of diffractions	1	—
$L_r^{\max}$	Max relative pathloss	40	dB
$\epsilon_{r,g}$	ground relative permittivity	16.06	—
σ_g	ground conductivity	0.397	S/m
$\epsilon_{r,b}$	building relative permittivity	5.31	—
σ_b	building conductivity	0.055	S/m
$\overline{\text{EIRP}}_{i,seg}$	average actual EIRP of ith segment	—	dBm

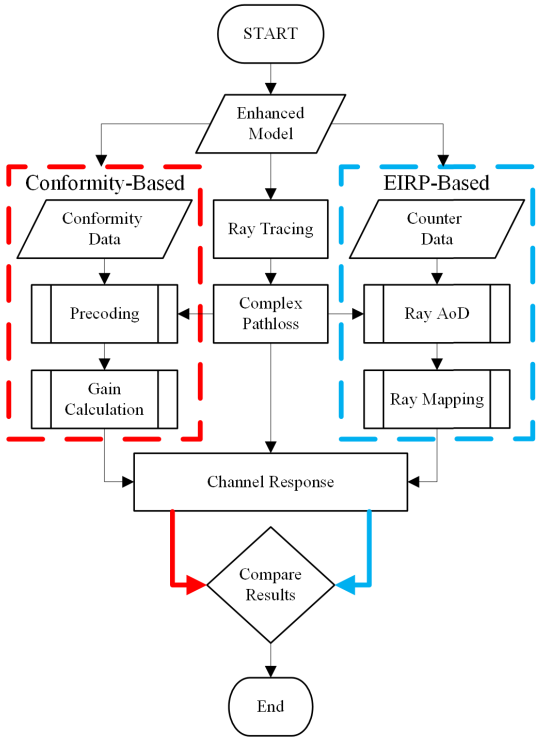

Figure 1. Simulation workflow of basic ray tracing and EIRP-based ray tracing processing blocks.

simulations, only the controlled UT is considered, while unknown UTs are excluded from the scope of this study. The environmental materials are restricted to concrete and loamy soil, selected based on the site's known soil composition with a typical Volumetric water content of 20% [21]. These materials are used to model the building structures and terrain, respectively. The relative permittivity and conductivity of loamy soil were calculated based on the "earthSurfacePermittivity" built-in MATLAB function [22], [23] and are listed along other simulation parameters in Table 1.

1) SIMULATION WORKFLOW

Figure 1 shows the overall simulation workflow for exposure assessment using both conformity-based and EIRP-based inputs. The process begins by using the enhanced site model shown in Figure 2 in Section II-A2 to perform RT simulations. For each EP, the contributing rays and their corresponding complex path loss are extracted based on the simulation parameters summarized in Table 1. The channel responses are generated based on the ray-tracing simulations at each EP.

Simulations with conformity-based inputs are based on [17] and employ maximum-ratio transmission (MRT) precoding as in [13], reflecting the reciprocity-based beamforming of the BSA [24]. The precoder generates the radiation pattern at each EP, and intersecting the traced rays with this pattern yields the required per-ray transmit gains. This approach estimates the maximum simulated signal strength at each EP as formulated in Section II-A3.

As shown in Figure 3, the EIRP values are reported over discrete azimuth-elevation segments of the BSA field of view (FoV). Each ray is generated with a known angle of departure (AoD), and this AoD is mapped to the corresponding FoV segment. The rays are then assigned the time-averaged EIRP reported for that segment, ensuring that the transmitted rays collectively reproduce the antenna's directional power distribution. When multiple rays occupy the same directional segment, the segment's total energy is divided among them to satisfy energy-conservation requirements, following the formulas described in Subsection II-A3. The received E-field is then obtained from the channel's response to each specific group of inputs for both processing blocks.

2) 3D MODEL AND OPTIMAL SETTINGS

As shown in Fig. 2 (Left), OpenStreetMap (OSM) [25] provides basic building models; however, their detail is often insufficient for RT simulations, which are highly sensitive to geometric accuracy [26]. To improve fidelity, an initial simulation using OSM data identifies structures interacting with rays at each EP. All buildings involved in any interaction are then selectively refined in Blender [27], as illustrated in Fig. 2 (Right). The refinements are limited to building height, rooftop type, and adjustments to unique buildings (the sport hall beside the BSA tower). This refinement process can be iteratively repeated when newly refined

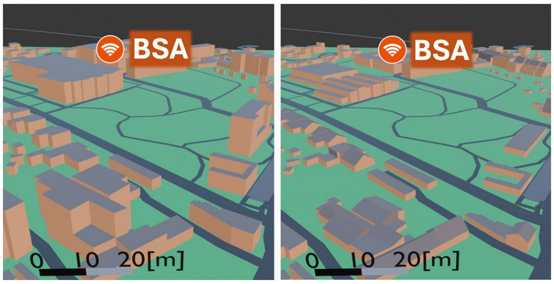

Figure 2. **Representation of (Left) the openstreetmap (OSM) model imported using blosm add-on in blender [25], and (Right) the refined model. The BSA is located beside the sports hall.**

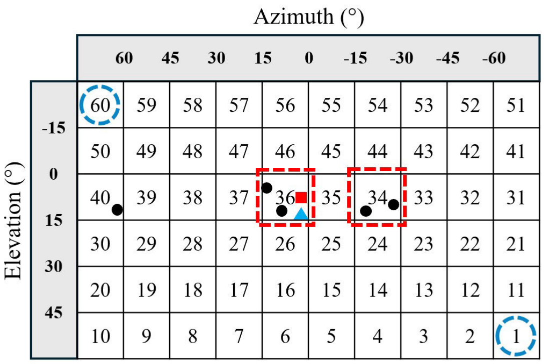

Figure 3. **The segmentation of the EIRP data in elevation (positive values represent downtilt) and azimuth with an example ray set. The red square, blue triangle, and black circles represent the LOS, ground reflection and reflected and/or diffracted rays, respectively. The dashed squares show ray groups that share the same EIRP data.**

buildings introduce additional propagation paths, ensuring a progressively accurate and realistic 3D model.

A setting that considers up to 5 reflections and a single diffraction was found to provide sufficient accuracy even under non-line-of-sight (NLOS) conditions [28].

3) PROCESSING BLOCK FORMULATION

In MATLAB [18], the built-in "sigstrength" function evaluates the signal strength at a receiver's location based on transmitter's output power (P_{TX} in [W]) among other parameters as listed in Table 1. The formulation starts with (1), where the radiated power density (S_{TX}) is calculated at a distance (r) from the transmitter, considering a lossless transmitter with P_{TX}, gain (G_{TX} in linear scale), and propagation factor (F_p=1 for homogenous medium) accounting for the scenario complexity.

$$S_{TX} = \frac{P_{TX}\, G_{TX}\, F_p^2}{4\pi r^2} \tag{1}$$

The path loss (PL) can be expressed as shown in (2) and by substituting it into (1), we derive the formulation presented in (3a). Furthermore, under free-space conditions, the transmitted power is related to the root-mean-square (RMS) of E-field strength as described by (3b).

$$\mathrm{PL}(r) = \left(\frac{4\pi r}{\lambda_c F_p}\right)^2 \tag{2}$$

$$S_{\mathrm{TX}} = P_{\mathrm{TX}}\, G_{\mathrm{TX}} \left(\frac{4\pi}{\lambda_c^2}\right)\left(\frac{1}{\mathrm{PL}(r)}\right) \tag{3a}$$

$$S_{\mathrm{TX}} = \frac{1}{\eta}\,|E_{\mathrm{rms}}|^2 \tag{3b}$$

Thus, the transmitted E-field strength at the EP, denoted as E_{TX} can be calculated using (4), as follows:

$$E_{\mathrm{TX}}(r) = \sqrt{\eta P_{\mathrm{TX}} G_{\mathrm{TX}} \left(\frac{4\pi}{\lambda_c^2}\right)\left(\frac{1}{\mathrm{PL}(r)}\right)} \tag{4}$$

$$E_i(r) = \sqrt{\frac{\eta\, 4\pi}{\lambda_c^2}}\sqrt{P_{\mathrm{TX}}}\sqrt{G_{\mathrm{TX},i}}\sqrt{\frac{1}{\mathrm{PL}_i(r)}} \tag{5a}$$

$$E_i(r) = \sqrt{\frac{\eta\, 4\pi}{\lambda_c^2}}\sqrt{\frac{\mathrm{EIRP}_{i,seg}}{N_i}}\sqrt{\frac{1}{\mathrm{PL}_i(r)}} \tag{5b}$$

In (5a) and (5b), the only unknown variable is the ray-specific complex path loss (PL_i) representing field attenuation, which is obtained from the RT simulation. To compute the superposition of all contributing rays at an EP, the E-field components (E_i) for the rays are derived using (5a) for the conformity inputs and (5b) for the EIRP inputs, respectively. Figure 3 shows an example of the grouped rays that share the same EIRP value which should be considered in 5b.

In the processing block for conformity data, the gain of i-th ray ($G_{\mathrm{TX},i}$) is calculated based on the precoding array and AoD for each ray. In the processing block for EIRP data, N_i accounts for the number of rays directed toward the same segment, thereby ensuring energy conservation. The equal division of energy between the rays inside a segment is an approximation which provides a sample of the power and gain in the direction of the ray over the duration of the measurement. Since the rays are not physical energy carriers, this leads generally to an overestimation of exposure levels. The E_{i} components are complex values because of the complex path loss derived from ray tracing. Finally, the E-field strength [dBμV/m] at an EP, is determined by computing the amplitude of the superposition of all contributing rays as follows:

$$E_{\mathrm{RX}} = 120 + 20 \times \log\left(\left|\sum_{i=1}^{N_{ray}} E_i\right|\right) \tag{6}$$

In addition to the EIRP-based RT results, to conservatively estimate the maximum exposure from EIRP data for the worst-case scenario, we rescale the EIRP segment values to the maximum allowed EIRP using conformity specifications [17] at 67.7 dBm, assuming maximum gain and power allocation.

B. IN-SITU MEASUREMENTS

The measurements were conducted in Ghent, Belgium, within an operational 5G network environment characterized by dynamic conditions, including the effects of beamforming

Table 2. Setup and settings for in-situ measurements.

Symbol	Description	Value	Unit
BW	bandwidth of interest	3.7–3.8	GHz
RBW	resolution bandwidth	100	kHz
Δt	routine duration	6	min
st	sweep time	110	ms
sp	sampling period	$\sim 3 \times st$	ms
h_{probe}	probe height	1.5	m
h_{phone}	phone height	1.5	m
E_{SA}	E-field strength in SA	Actual	dBμV/m
sensitivity	SA sensitivity at EP	—	dBμV/m

and varying user traffic. The validation performed in this study is limited to LOS scenarios. The measurements adhere to the IEC 62232 standard [9].

The equipments used for the in-situ measurement routines include: NARDA SRM-3006 (SRM), (optional: other devices as listed in [29], may also be employed for EMF exposure assessment.) triaxial broadband probe (3502/02), RF-Cable (3602/02), wooden or plastic tripods, phone equipped with QualiPoc [30] for link monitoring and validation. (A device capable of maintaining a DL connection is sufficient for the measurements.) The reported expanded uncertainty of the SRM device in this configuration is 1.9 dB (with a coverage factor k=2) within the bandwidth of interest [27]. Measurement consistency is ensured through multiple repetitions at the same EP for FTP-DL measurements. In Table 2, the measurement settings for the FTP-DL routine are summarized. During the 6-minute in-situ measurement, the UE repeatedly requests a 10 GB file download to maintain a continuous DL connection with the 5G BSA. The SRM operates at the finest resolution bandwidth (RBW) of 100 kHz, to maximize sample capture. Sweep time (st) is internally computed based on bandwidth, RBW, and processing requirements, while the sampling period (sp) is limited by the serial port baud rate. Device sensitivity is adjusted on-site to prevent saturation and ensure accurate EMF measurements.

1) DATA COLLECTION AND PROCESSING

The measurement duration and scheduling are governed by the sampling interval of the BSA counters, which report the 6-minute average EIRP per segment ($\overline{EIRP}_{\text{seg}}$) values every 5 minutes. The recorded data with the SRM corresponds to frequency samples for actual E-field strength (E_f^{act}) at the location of the probe, expressed in $dB\mu V/m$. The frequency samples are processed according to (7) to compute the channel E-field strength (E_{ch}^{act}) where a sweep index (SI) of 2 is applied, indicating that the sweep filter spans two frequency sample points, and thus the power is effectively recorded twice by the SRM.

$$E_{\text{ch}}^{\text{act}} = \sqrt{\frac{1}{\text{SI}} \sum_{f=1}^{N_f} E_f^{act\,2}} \tag{7}$$

For comparison with simulations, the 6-minute average of the $E_{\text{ch}}^{\text{act}}$ samples are calculated by dividing the overall power by the number of samples (N_t) for each in-situ measurement.

$$\overline{E}_{\text{ch}} = \sqrt{\frac{1}{N_t} \sum_{t=1}^{N_t} E_{ch}^{act\,2}} \tag{8}$$

Data cleaning was performed based on outlier detection during the data processing phase, supported by the time-series visualization shown in Fig. 6 and the QualiPoc reports. In a few cases, the UT connection was disrupted, namely the EP and ID pairs of (2,1), (2,4), (3,2), (5,6), which have been omitted in Section III-E.

2) UNCERTAINTY ANALYSIS

The identified sources of uncertainty primarily stem from the highly dynamic behavior of wireless networks, specifically the adaptation of beamforming, power control, and scheduler allocation in response to user mobility and activity, as well as from environmental variations that further affect the resulting EMF exposure levels. The effects of uncertainty from noise and short-term traffic variation are mitigated through averaging. For long-term traffic variation and beam directionality, the application of the FTP-DL routine helps reduce measurement uncertainty through stabilizing the resource allocation and ensures the activation of beamforming used in 5G MaMIMO BSAs. Consequently, the dominant sources of uncertainty are captured within the measured data. For in-situ measurements, the measurement data are treated as Type A (u_A) source of uncertainty, while the device and setup-related uncertainties are classified as Type B (u_B). These are then combined to calculate the overall uncertainty [31]. Given the skewed distribution observed in the in-situ measurement results (Fig. 9), a bootstrap approach is employed to estimate the associated uncertainty. To compute the combined uncertainty, the bootstrap-derived distribution is convolved with a zero-mean normal probability density function (PDF), which represents the setup-related uncertainty as characterized in [27]. This procedure yields the 95th percentile confidence interval (CI) for the measurements, as presented in Table 6.

3) FTP-DL MEASUREMENT

In Fig. 4, the selected LOS EPs are indicated by blue markers for UT placement and by the red marker for the 5G antenna. Also, Fig. 4 includes an example for the location sensitivity grid and the in-situ measurement setup. For the FTP-DL measurement, the phone is placed at a distance of $d_p = 2\ m$ from the probe as recommended in [14]. Other relevant parameters are provided in Table 2. The in-situ measurements were performed between 09/04/2025 and 09/05/2025.

4) SSS-BASED EXTRAPOLATION

Measurements of the Secondary Synchronization Signal (SSS) are performed at the same EPs as in the FTP-DL setup (Fig. 4) and repeated for 2 or 3 times, using the

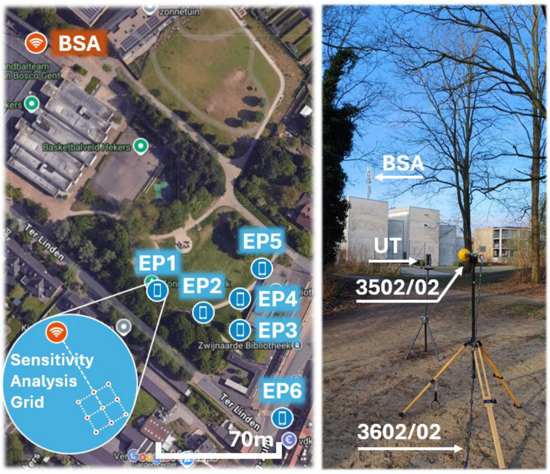

Figure 4. The measurement map for the FTP-DL routine and an example of the in-situ measurement setup. The blue markers indicate the evaluation points, while the red marker represents the BSA. The example grid shows the relative positions for the location sensitivity simulations with steps of 2 meters.

Table 3. In-situ description and information of the evaluation points for FTP-DL measurements.

EP	LOS Condition	Description	Dist.[m]
1	trees in LOS	in the vicinity of a tree	160
2	trees in LOS	pathwalk crossing	183
3	trees in LOS	between two buildings	204
4	trees in LOS	10 m away from a building	191
5	trees in LOS	4 m away from a building	185
6	tram/trees in LOS	busy roadside and crosswalk	260

5G mode of the NARDA SRM-3006. This mode enables code-selective detection of SSS, requiring prior knowledge of subcarrier spacing (SCS) and PBCH center frequency as listed in Table 4 [27]. To confirm connection to the BSA under study, drive test tools (e.g. QualiPoc) are used to extract the cell-ID and compare it to SSS-specific measurement data. The 2-minute average electric field strength in mV/m is recorded across all broadcast beams at the EPs, including those from adjacent subsectors. These measurements help with EMF exposure estimation through extrapolation and distinguish between static broadcast beam and dynamic traffic beam exposure, which cannot be captured without full BSA control.

The average power of resource elements (REs) depends on the number of resource blocks used in the signal. The PSS, SSS, and PBCH occupy one symbol in time domain and 127, 127, and 240 subcarriers in frequency domain, respectively. To derive the average E-field strength per RE ($\overline{E}rms, RE$), the 2-min averaged E-field strength ($\overline{E}rms, meas$) is normalized by the number of subcarriers (N_{sc}), as shown in (9). Note that the averaged E-field strength ($\overline{E}_{rms,meas}$) only accounts for the dominant beam corresponding in the EP's subsector, as contributions from the remaining beams are negligible (typically 10 to 20 times lower).

$$\overline{E}_{rms,RE} = \frac{\overline{E}_{rms,meas}}{\sqrt{N_{sc}}} \tag{9}$$

The overall extrapolation factor from SSS-based measurements to maximum exposure can be derived using (9), equation (E.16) of [9], and the parameters listed in Table 4.

Table 4. SSS-based measurement settings and extrapolation parameters of E.16 referenced in [9].

Symbol	Description	Value	Unit
f_c	center frequency of PBCH block	3.75024	GHz
SCS	subcarirrer spacing	30	kHz
BW	signal bandwidth	100	MHz
sp	sampling period	120	s
st	sweep time	2.5	s
F_{BW}	total carrier bandwidth to subcarrier frequency spacing of SSB ratio	12×273	—
F_{PR}	power reduction for actual maximum approach	1	—
F_{TDC}	technology duty cycle	75%	—
F_B	transmitted power ratio of broadcast to traffic beam	1	—

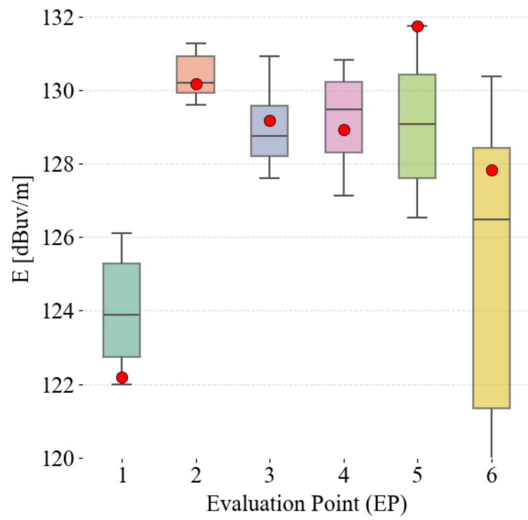

Figure 5. Sensitivity of RT simulations to location accuracy using a 2-meter grid step around the median GPS coordinates of the EPs. The red dots represent the value at the center point.

5) PEAK-TO-AVERAGE RATIO

The Peak-to-Average Ratio (PAR) is a valuable metric for assessing exposure variability, particularly in scenarios where peak levels rather than average values may drive biological effects [4], [24]. Different technologies and use cases may exhibit distinct PAR characteristics, i.e. 2 for a sinusoidal signal, 8.7 for GSM, 3.1–3.3 for UMTS-FDD, 10–20 for WLAN [32]. Possible ranges for PAR are constant exposure (PAR $\approx$ 1), mildly varying exposure ($1 < PAR < 3$), dynamic exposure ($3 < PAR < 10$), and extreme exposure ($PAR > 10$ or ∞).

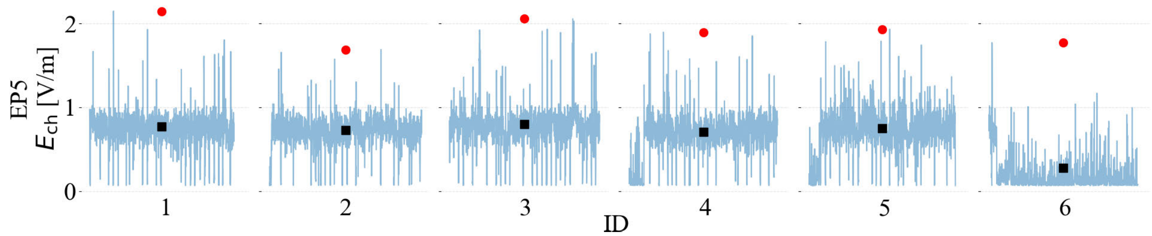

Figure 6. Example of the measured channel E-field (E_{ch}) levels (EP5) for different measurements over time. The maximum and time-averaged (6 min) E-field values are denoted as $E_{ch}\max$ (red circular dots) and $\overline{E}_{ch}$ (black square dots), respectively and are overlaid on the plots.

III. RESULTS

A. LOCATION SENSITIVITY IN SIMULATIONS

Fig. 5 shows the simulated E-field strength of the conformity-based inputs on the sensitivity grid visualized in Fig. 5. As shown, the results are highly sensitive to location accuracy, due to multipath propagation effects arising from phase differences and power variations of individual rays. Specifically, Fig. 5 shows that they are highly sensitive in cases of EP1, EP5, and EP6, where the IQR is larger than 2, 3, and 6 dB, respectively. Detailed analysis indicate that the LOS and ground-reflection (GR) rays dominate, contributing 88.3% to 99.9% of the received power across EPs. At EP1, EP2,and EP4, variations arise from LOS to GR phase differences, where EP1 shows destructive interference and a larger IQR, while EP2 and EP4 exhibit constructive interference. At EP5 and EP6, additional rays contribute 9% to 11.7%, increasing power variation and IQR. Random phase differences between the rays of each EP would yield much larger IQR spans (>30 dB).

B. SPATIO-TEMPORAL ANALYSIS IN MEASUREMENTS

During the in-situ measurements, 8–11 unknown UTs were connected to the antenna, and no traffic-load information was available. Resource sharing among them could reduce signal strength by up to 10.4 dB compared to a single-user scenario, which serves as a lower bound for BSA-induced reduction relative to maximum single-user exposure.

Fig. 6 shows the measured channel E-field (E_{ch}) samples for an example EP5 and different measurement identifications (IDs). Considering all measurement data, the E_{ch} samples show a high variability with a coefficient of variation (CV = standard deviation / mean) ranging from 29% to 49.7% and do not follow a predictable pattern. In a few specific cases namely (EP, ID) pairs of (2,4), (3,2), and (5,6), the QualiPoc established link was disrupted, which led to significantly lower E_{ch} samples. Under stable conditions with consistently active UTs, the time-averaged channel E-filed ($\overline{E}_{ch}$) remains highly stable (variation <1 dB) across all EPs over six consecutive measurements within one hour. In contrast, the peak values vary noticeably across EPs, with CVs from 9% to 19%, reflecting strong fluctuations. The highest recorded peak was approximately 2.8 V/m, observed at EP1. Furthermore, the maximum E-field values tend to decrease from 2.8 V/m to 1 V/m with increasing distance from EP1 to EP6.

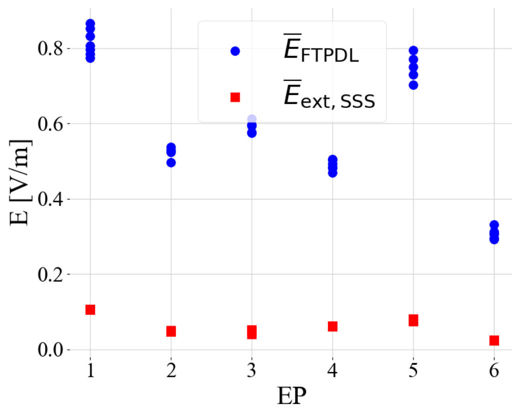

Figure 7. An E-field strength comparison between the partial extrapolation (without F_B factor) of the broadcast beam and the FTP-DL measurements across EPs. Measured values were averaged over 2-min for broadcast beam and over 6-min for the FTP-DL routine.

C. SSS-BASED EXTRAPOLATION

Fig. 7 shows the E-field strength comparison of the SSS-based extrapolation (assuming the factors in Table 4) and FTP-DL measurement routine. Sequential SSS-based estimations exhibit negligible variation across EPs. The 2-min averages of broadcast-beam E-fields range from 25.5 mV/m at EP1 to 6.7 mV/m at EP6. The mean absolute error of 8.5–10.3 dB across EPs quantifies the difference between the assumed extrapolation factors and real-world maximum exposure.

D. PEAK-TO-AVERAGE RATIO

Fig. 8 shows the peak-to-average ratio (PAR) for the FTP-DL measurements. As shown, the majority of measurements fall within a PAR range of 2 to 3, indicating moderate signal fluctuations. Values exceeding this range can be attributed to specific conditions involving either high peak bursts or low average exposure levels. For the (EP, ID) pairs (1,5) and (1,7), elevated PAR values are primarily due to high-peak bursts of 2.7 V/m and 2.8 V/m, respectively. In contrast, pair

Table 5. **Summary of datasets used for comparative analysis.**

Dataset	Description	Values per EP	Expanded Uncertainty (k=2)	Derived Statistics
RT with $\overline{EIRP}_{act}$	Ray tracing with 6-minute averaged actual EIRP values	6	—	Median (IQR)
In-situ Measurements	Measured 6-minute averaged E-field strength	6	u_A and 1.9 dB	Median (IQR)
RT with rescaled EIRP input to EIRP_{MAX}	Ray tracing with rescaled EIRP values to EIRP_{MAX} (67.7 dBm) as worst-case scenario	6	—	Median (IQR)

Table 6. **Comparison of simulation and measurement results per evaluation point (EP).**

EP	RT	$\mathrm{EIRP\text{-}RT}_{\mathrm{MAX}}$		EIRP-RT		Measurement			$\Delta\tilde{x}$[dB]	Comments
		Median	IQR	Median	IQR	Median	IQR	u_C (95% CI)		
EP1	122.20	118.78	0.03	116.57	0.39	118.57	0.56	3.78	1.56	Good agreement
EP2	129.19	122.32	0.06	118.20	2.99	114.44	0.23	3.72	-3.76	Overestimation
EP3	128.93	122.21	0.01	117.70	1.65	115.48	0.30	3.80	-2.22	Overestimation
EP4	130.18	120.11	0.02	117.24	0.67	113.79	0.34	3.79	-3.45	Overestimation
EP5	131.76	119.92	2.37	114.62	2.22	117.50	0.47	3.88	2.88	Underestimation
EP6	127.83	114.21	0.10	112.40	0.52	109.73	0.36	3.80	-2.68	Overestimation

* All values are reported in $\mathrm{dB}\mu\mathrm{V/m}$ unless explicitly indicated otherwise.

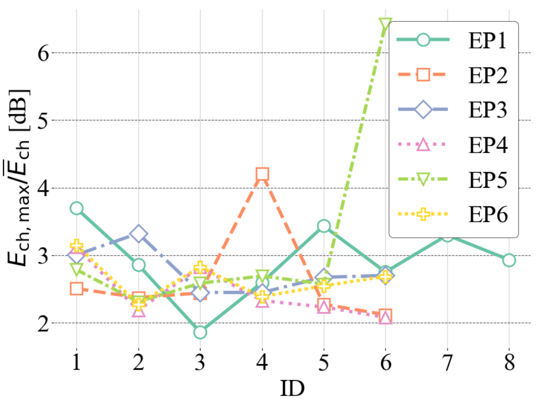

Figure 8. **Peak-to-Average Ratio ($\frac{E_{ch,max}}{\overline{E}_{ch}}$) of channel E-field strength (E_{ch}) for evaluation point (EP) and measurement identification (ID).**

(1,1) shows a PAR above 3 due to its low average channel exposure ($\overline{E}_{ch} = 0.5$ V/m), with consistently weak signals throughout the measurement period. Further analysis of the EIRP data indicated that the BSA operated at reduced power, likely due to serving users distributed over a wider coverage area. Additionally, pairs (2,4), (3,2), and (5,6) exhibit high PAR values due to low $\overline{E}_{ch}$ levels during QualiPoc disruptions 0.33 V/m, 0.35 V/m, and 0.28 V/m, respectively.

E. GENERAL COMPARISONS

Fig. 9 compares EIRP-based simulations with in-situ FTP-DL measurements across all EPs. Table 5 summarizes the dataset used for this comparison. The three boxplots per EP represent: (1) simulations using actual EIRP, (2) in-situ measurements, and (3) simulations using rescaled EIRP. The green bands, centered on the in-situ medians, show the combined measurement and setup uncertainty (u_C, 95% CI). The median difference between measurements ($\tilde{x}_{meas}$) and actual-EIRP simulations ($\tilde{x}_{EIRP}$) is indicated at the bottom for each EP ($\Delta\tilde{x} = \tilde{x}_{meas} - \tilde{x}_{EIRP}$ [dB]). Key numerical results are listed in Table 6. Overall, EIRP-based simulations partly overlap with the in-situ uncertainty range and generally overestimate exposure. At EP1 and EP5, simulations underestimate exposure, caused respectively by destructive interference (EP1) and low recorded EIRP values, where the BSA covered an adjacent area (EP5). Using rescaled EIRP (third boxplot group), simulations overestimate exposure at all EPs, with overlap only at EP5, consistent with its large IQR (2.5 dB) indicating unreliable EIRP data. While operator-provided EIRP counter uncertainties are unknown, Fig. 9 shows that EIRP-based medians still align reasonably with measurements, differing by 1.6 to 3.8 dB. The 1.9 dB (k=2) figure reflects only equipment uncertainty. In line with [9], assuming a 4 dB expanded uncertainty places the EIRP-based medians within the acceptable in-situ range.

F. INTER-STUDY COMPARISON

In Table 7, a comparison of the findings of this study and similar studies has been summarized. Most existing studies focus exclusively on simulations [13] or solely on in-situ measurements [10], [11], [12], without combining the two approaches. In contrast, this study integrates both simulation and measurement methodologies, as reflected in Table 7. We introduce an adjusted processing block for RT simulations that incorporates EIRP data recorded from an operational 5G network as formulated in II-A3. This allows the simulation to account, at least partially, for dynamic beamforming,

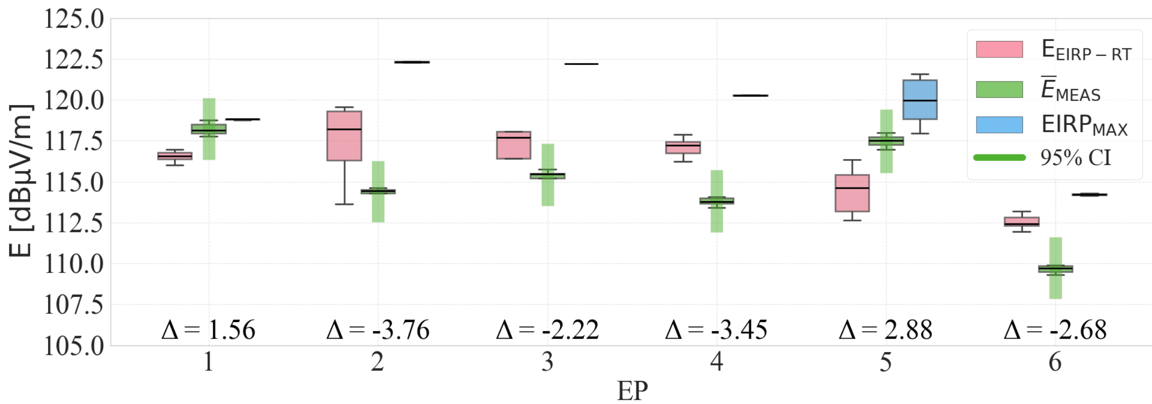

Figure 9. A comparison between the EIRP-based RT results, in-situ measurements, and the rescaled EIRP-based RT results ($EIRP_{MAX}$) for each EP. A green bar centered on the median of the in-situ measurements represent the expanded uncertainty estimation considering the setup uncertainty of 1.9 dB (k=2) and measurement data uncertainty. The difference between the medians of the in-situ measurements and the EIRP-based results are overlaid above the horizontal axis and noted with Δ.

Table 7. Comparison of EMF exposure assessment literature in 5G environments.

Reference	Method	Scenario	Reported Error (value)	ICNIRP limit [%]
[13]	RT + Static Power	Urban, 5G DL	—	4
[10]	Measurement	Outdoor, 5G	—	7.7
[33]	PMI + RT	outdoor / stadium interior, 5G MaMIMO	—	95% = 7.6
[12]	Spot Meas., Extrapolation	outdoor, 5G MaMIMO	$\epsilon = 0.2\ V/m$	0.5 to 0.6
[11]	Spot Meas., Extrapolation	outdoor, 5G	—	0.0005–5
This work	EIRP-based RT	Urban, 5G MaMIMO	$\bar{\epsilon}_{abs} = 2.76\ dB$	max at 0.035
This work	$EIRP_{max}$-based RT	Urban, 5G MaMIMO	$\bar{\epsilon}_{abs} = 4.5\ dB$	—
This work	Conformity-based RT	Urban, 5G MaMIMO	$\bar{\epsilon}_{abs} = 13.65\ dB$	max at 0.6

power control, varying traffic loads, user distribution, and environmental conditions. The resulting E-field estimates are evaluated against in-situ measurements while considering both the target and limit expanded uncertainties defined in [9], an aspect often absent in comparable publications. A related study in [33] also employs EIRP data for exposure estimation, although using different commercial software. However, our work distinguishes itself by evaluating multiple points with diverse surrounding conditions. Each EP exhibits a distinct set of contributing rays, providing deeper insight into the variability of E-field estimation and the influence of local propagation characteristics. Additionally, the investigated methods in this work have been compared to the ICNIRP limits at FR1 for a maximum of 0.6 %.

IV. CONCLUSION

Ray-tracing simulations and in-situ measurements were performed and compared across six LOS EPs, including their associated measurement uncertainty. The RT results were found to be highly sensitive to location precision at the test site. In-situ measurements showed that during FTP-DL routines, exposure levels did not follow a simple distance-dependent trend, indicating the influence of additional variables and the relevance of advanced modelling. The low interquartile range (< 0.5 dB) across repeated measurements demonstrated high stability in the measurement procedure. The resulting expanded uncertainty of the measurements remained within the 4 dB target. Extrapolated broadcast-beam measurements revealed a missing contribution of combined extrapolation factors, ranging between 8.5 and 10.3 dB, needed to match the averaged E-field strength of the FTP-DL measurements. Comparison between EIRP-based simulations and in-situ results showed deviations in the range of -2.9 dB to +3.8 dB in median values across EPs with a few exceptions due to disrupted protocol. Based on this, careful consideration is required when comparing the estimations to reference levels, as there remains a potential for underestimating actual exposure. In this study the recorded and simulated EMF exposure levels fall well below the ICNIRP levels with a maximum at 0.6 % of the limits for FR1. Future work should focus on enhancing RT accuracy through higher-resolution, dynamic environment modelling that incorporates trees, vehicles, and more realistic physical phenomena (e.g., refraction and scattering). Measurement strategies could be broadened to cover alternative traffic patterns and multi-user scenarios. Finally, extending the investigation across diverse microenvironments and under NLOS conditions would provide a more complete picture of exposure variability.

ACKNOWLEDGMENT

Views and opinions expressed are however those of the authors only and do not necessarily reflect those of the European Union or the Health and Digital Executive Agency.

Neither European Union nor the granting authority can be held responsible for them. The authors would like to thank Jeroen Van Der Straeten for helping with the in-situ validation measurements.

References

[1] T. L. Marzetta, E. G. Larsson, H. Yang, and H. Q. Ngo, *Fundamentals Massive MIMO*. Cambridge, U.K.: Cambridge Univ. Press, 2016.

[2] E. Björnson, J. Hoydis, and L. Sanguinetti, ''Massive MIMO networks: Spectral, energy, and hardware efficiency,'' *Found. Trends Signal Process.*, vol. 11, nos. 3–4, pp. 154–655, Nov. 2017.

[3] A. Hirata, Y. Diao, T. Onishi, K. Sasaki, S. Ahn, D. Colombi, V. De Santis, I. Laakso, L. Giaccone, W. Joseph, E. A. Rashed, W. Kainz, and J. Chen, ''Assessment of human exposure to electromagnetic fields: Review and future directions,'' *IEEE Trans. Electromagn. Compat.*, vol. 63, no. 5, pp. 1619–1630, Oct. 2021.

[4] International Commission on Non-Ionizing Radiation Protection (ICNIRP). (2020). *ICNIRP Guidelines for Limiting Exposure to Electromagnetic Fields (100 kHz to 300 GHz)*. [Online]. Available: https://www.icnirp.org/en/activities/news/news-article/RF-guidelines-2020-published.html

[5] *IEEE Standard for Safety Levels With Respect to Human Exposure to Electric, Magnetic, and Electromagnetic Fields, 0 Hz to 300 GHz*, Standard C95.1-2019, 2019. [Online]. Available: https://standards.ieee.org/ieee/C95.1/4940/

[6] World Health Organization. *Electromagnetic Fields*. Accessed: Oct. 10, 2025. [Online]. Available https://www.who.int/health-topics/electromagnetic-fields#tab=tab_1

[7] World Health Organization. *The International EMF Project*. Accessed: Oct. 10, 2025. [Online]. Available: https://www.who.int/initiatives/the-international-emf-project

[8] A. Elzanaty, L. Chiaraviglio, and M.-S. Alouini, ''5G and EMF exposure: Misinformation, open questions, and potential solutions,'' *Frontiers Commun. Netw.*, vol. 2, pp. 5–8, Apr. 2021.

[9] *Determination of RF Field Strength and SAR in the Vicinity of Radiocommunication Base Stations for the Purpose of Evaluating Human Exposure*, document IEC 62232:2025, International Electrotechnical Commission, 2025. [Online]. Available: https://webstore.iec.ch/en/publication/89073

[10] K. Deprez, L. Verloock, L. Colussi, S. Aerts, M. Van den Bossche, J. Kamer, J. Bolte, L. Martens, D. Plets, and W. Joseph, ''In-situ 5G NR base station exposure of the general public: Comparison of assessment methods,'' *Radiat. Protection Dosimetry*, vol. 198, no. 6, pp. 358–369, May 2022.

[11] C. Calderon, D. Addison, and A. Peyman, ''In-Situ measurements of radiofrequency electromagnetic fields measurements around 5G macro base stations in the U.K.,'' *Bioelectromagnetics*, vol. 46, no. 5, p. 70012, Jul. 2025.

[12] S. Aerts, K. Deprez, D. Colombi, M. Van den Bossche, L. Verloock, L. Martens, C. Törnevik, and W. Joseph, ''In situ assessment of 5G NR massive MIMO base station exposure in a commercial network in Bern, Switzerland,'' *Appl. Sci.*, vol. 11, no. 8, p. 3592, Apr. 2021.

[13] M. Leeman, R. Wydaeghe, J. van der Straeten, S. Goegebeur, G. Vermeeren, and W. Joseph, ''City-scale spatio-temporal modeling of 5G downlink exposure of users and non-users by ray-tracing in a real urban environment,'' *IEEE Access*, vol. 13, pp. 30894–30906, 2025.

[14] Y. Li, Z. Li, Z. Gao, and T. Chen, ''Geo2SigMap: High-fidelity RF signal mapping using geographic databases,'' in *Proc. IEEE Int. Symp. Dyn. Spectr. Access Netw. (DySPAN)*, Washington, DC, USA, May 2024, pp. 277–285.

[15] D. Colombi, P. Joshi, B. Xu, F. Ghasemifard, V. Narasaraju, and C. Törnevik, ''Analysis of the actual power and EMF exposure from base stations in a commercial 5G network,'' *Appl. Sci.*, vol. 10, no. 15, p. 5280, Jul. 2020.

[16] Vlaamse Overheid. *Kaart Zendantennes*. Accessed: Oct. 10, 2025. [Online]. Available: https://omgeving.vlaanderen.be/nl/onderzoek-cijfers-en-geoloketten/cijfers-en-kaarten/kaart-zendantennes

[17] Vlaamse Overheid. *Conformiteitsattest Zendantennes*. Accessed: Oct. 10, 2025. [Online]. Available: https://zendantennes.omgeving.vlaanderen.be/publiek/dossier/285782429/conformiteitsattest

[18] MathWorks. (2023). *Ray Tracing Propagation Mode*. [Online]. Available: https://www.mathworks.com/help/antenna/ref/rfprop.raytracing.html

[19] MathWorks. *Antenna Toolbox*. Accessed: Oct. 10, 2025. [Online]. Available: https://nl.mathworks.com/products/antenna.html

[20] MathWorks. *Phased Array System Toolbox*. Accessed: Oct. 10, 2025. [Online]. Available: https://nl.mathworks.com/products/phased-array.html

[21] Vlaamse Overheid. *Bodemverkenner*. Accessed: Oct. 10, 2025. [Online]. Available: https://www.dov.vlaanderen.be/portaal/?module=public-bodemverkenner

[22] *Earthsurfacepermittivity*, MathWorks Inc., Natick, MA, USA, 2022. [Online]. Available: https://www.mathworks.com/help/comm/ref/earthsurfacepermittivity.html

[23] *Electrical Characteristics of the Surface of the Earth*, document Recommendation ITU-R p.527, International Telecommunication Union Radiocommunication Sector, Sep. 2021. [Online]. Available: https://www.itu.int/rec/R-REC-P.527/en

[24] K. Gopala and D. Slock, ''Reciprocity-based beamforming techniques for spectrum sharing in MIMO networks,'' in *Proc. Spectr. Sharing, Next Frontier Wireless Netw.*, Oct. 2020, pp. 169–190.

[25] OpenStreetMap contributors. (Oct. 2023). *Planet Dump*. [Online]. Available: https://planet.openstreetmap.org

[26] Blender Online Community. (2023). *Blender—A 3D Modelling and Rendering Package, Version 3.1.0*. Stichting Blender Foundation. [Online]. Available: https://www.blender.org

[27] Narda STS. *SRM Datasheet*. Accessed: Oct. 10, 2025. [Online]. Available: https://www.narda-sts.com/index.php?eID=dumpFile&t=f&f=1474&dl=1&token=724573573771fe00e45c3e2a48f652174de7d844

[28] G. E. Athanasiadou and A. R. Nix, ''Investigation into the sensitivity of the power predictions of a microcellular ray tracing propagation model,'' *IEEE Trans. Veh. Technol.*, vol. 49, no. 4, pp. 1140–1151, Jul. 2000.

[29] E. Korkmaz, S. Aerts, R. Coesoij, C. R. Bhatt, M. Velghe, L. Colussi, D. G. Land, N. E. Petroulakis, M. Spirito, and J. Bolte, ''A comprehensive review of 5G NR RF-EMF exposure assessment technologies: Fundamentals, advancements, challenges, niches, and implications,'' *Environ. Res.*, vol. 260, Oct. 2024, Art. no. 119524. [Online]. Available: https://www.sciencedirect.com/science/article/pii/S0013935124014294

[30] Rohde & Schwarz. *Qualipoc Android–Smartphone-Based Mobile Network Testing Solution*. Accessed: Oct. 10, 2025. [Online]. Available: https://www.rohde-schwarz.com/product/qualipoc_android

[31] *Evaluation of Measurement Data—Guide to the Expression of Uncertainty in Measurement*, document JCGM 100:2008, Joint Committee for Guides in Metrology (JCGM), 2008.

[32] National Center for Biotechnology Information. *Biological Effects of EMF*. Accessed: Oct. 10, 2025. [Online]. Available: https://www.ncbi.nlm.nih.gov/books/NBK304624/

[33] C. D. Paola, P. Joshi, D. Colombi, B. Xu, J. E. Bischoff, S. S. Zhekov, and C. Törnevik, ''Network-based assessment of actual EIRP of 5G base stations in a stadium with 100 000 people and implications on EMF compliance,'' *IEEE Antennas Wireless Propag. Lett.*, vol. 24, pp. 242–246, 2025.

JAVAD HEIDARI (Graduate Student Member, IEEE) received the master's degree in electrical engineering from Tarbiat Modares University, Tehran, Iran. He is currently pursuing the Ph.D. degree with the WAVES Research Group, Department of Information Technology, IMEC, Ghent University, Ghent, Belgium. His research interests include numerical and experimental EMF exposure assessment in operational networks, including RF simulations, measurements, and calibration procedures for accurate exposure evaluation.

WOUT JOSEPH (Senior Member, IEEE) was born in Ostend, Belgium, in October 1977. He received the M.Sc. degree in electrical engineering and the Ph.D. degree from Ghent University, Ghent, Belgium, in July 2000 and March 2005, respectively. His Ph.D. work dealt with measuring and modeling of electromagnetic fields around base stations for mobile communications related to the health effects of exposure to electromagnetic radiation. From 2007 to 2012, he was a Postdoctoral Fellow with the Research Foundation Flanders (FWO-V), Brussels, Belgium. Since October 2009, he has been a Professor of experimental characterization of wireless communication systems. He has been a PI with IMEC, Ghent, since 2017. His professional interests include electromagnetic field exposure assessment, propagation for wireless communication systems, antennas, and calibration. Furthermore, he specializes in wireless performance analysis and quality of experience.

LUC MARTENS (Member, IEEE) received the M.Sc. degree in electrical engineering from Ghent University, Belgium, in July 1986, and the Ph.D. degree in December 1990. From September 1986 to December 1990, he was a Research Assistant with the Department of Information Technology (INTEC), Ghent University. During this period, his scientific work was focused on the physical aspects of hyperthermic cancer therapy. His research work dealt with electromagnetic and thermal modeling and with the development of measurement systems for that application. Since 1991, he has been managing the Wireless and Cable Research Group, INTEC. Since April 1993, he has been a Professor with Ghent University. He is currently a member with IMEC—WAVES Group, Department of Information Technology—INTEC, Ghent University. His experience and current interests are in modeling and measurement of electromagnetic channels, of electromagnetic exposure, e.g., around telecommunication networks and systems, such as cellular base station antennas, and of energy consumption in wireless networks. He is the author or co-author of more than 300 publications in the domain of electromagnetic channel predictions, dosimetry, exposure systems, and health and wireless communications.

GÜNTER VERMEEREN (Member, IEEE) is currently a Professor with the WAVES Research Group, Department of Information Technology, IMEC, Ghent University, Ghent, Belgium, where he is involved in the research on radio frequency dosimetry, electromagnetic exposure, and on-body propagation. He is the author of 57 publications in international journals and 54 papers at national and international scientific conferences. His research interests include numerical modeling (FDTD, MoM) as well as measurements of electromagnetic fields in the proximity of humans (exposure as well as on- and in-body propagation). His research results are also included in the international standard IEC 62232. Since 2013, he has also been involved in research on medical imaging systems with a focus on the modeling of the electromagnetic fields in hybrid MRI systems.